

## Effect of $\text{SO}_4^{2-}$ on the Corrosion Behavior of NiCu Low-Alloy Steel in Deoxygenated $\text{NaHCO}_3$ Solution (Postprint)

**Authors:** LU Yunfei, Dong Junhua, Ke Wei

**Date:** 2023-03-19T00:00:00+00:00

### Abstract

The effect of  $\text{SO}_4^{2-}$  on the corrosion behavior of NiCu low-alloy steel during immersion in deoxygenated  $\text{NaHCO}_3$  solution was investigated using in-situ electrochemical monitoring technique, and the phase structure of the corrosion product layer and surface morphology of the post-immersion samples were analyzed by XRD and SEM. The results show that, compared with pure  $\text{NaHCO}_3$  solution, the addition of  $\text{SO}_4^{2-}$  accelerates substrate corrosion at the initial stage of immersion, inhibits the formation of protective corrosion product film at later stages, and causes the corrosion mode to transform from pre-passivation behavior (in the absence of  $\text{SO}_4^{2-}$ ) to active dissolution. Furthermore, increased concentrations of both  $\text{SO}_4^{2-}$  and  $\text{HCO}_3^-$  facilitate the formation of  $\text{Fe}_6(\text{OH})_{12}\text{CO}_3$ . The corrosion products on the sample surface ultimately consist of  $\alpha\text{-FeOOH}$ ,  $\text{Fe}_3\text{O}_4$  and  $\text{Fe}_6(\text{OH})_{12}\text{CO}_3$ , and the surface morphology is dominated by uniform corrosion.

### Full Text

## Effects of $\text{SO}_4^{2-}$ on the Corrosion Behavior of NiCu Low Alloy Steel in Deaerated $\text{NaHCO}_3$ Solutions

LU Yunfei<sup>1, 2</sup>), DONG Junhua<sup>1</sup>), KE Wei<sup>1</sup>)

<sup>1</sup>) Environmental Corrosion Center, Institute of Metal Research, Chinese Academy of Sciences, Shenyang 110016

<sup>2</sup>) Wuhan the Second Ship Design and Research Institute, Wuhan 430064

**Correspondent:** DONG Junhua, professor, Tel: (024)23915912, E-mail: jh-dong@imr.ac.cn

**Supported by:** National Natural Science Foundation of China (No.51471175)

**Manuscript received:** 2015-03-10, in revised form 2015-06-28

## Abstract

High-level radioactive waste (HLW) represents an extremely hazardous by-product of the global nuclear industry. Due to its intensely radioactive nature and ultra-long half-life, HLW must be safely managed and isolated from the biosphere for thousands of years. Deep geological repository (DGR) is considered the most feasible option worldwide, relying on a multibarrier system comprising metallic canisters, backfill materials, and a stable geologic formation. Since radionuclides could migrate into the biosphere via groundwater action, both the geologic formation and backfill materials must exhibit very low hydraulic permeability, while metal canisters must resist corrosion and prevent groundwater contact with radioactive waste for as long as possible. Low-carbon steel has been studied as a candidate canister material in many countries due to its extensive industrial experience, high strength, and low cost, as well as its lower susceptibility to localized corrosion compared with passive materials. However, its higher corrosion rate may pose an insurmountable barrier to practical application.

Recent studies have revealed that NiCu low alloy steel is a more promising candidate for canister material compared with conventional low-carbon steel, as it demonstrates a more acceptable corrosion rate without substantially increasing cost and exhibits better resistance to localized corrosion in environments with high chloride concentrations. This work investigates the effects of  $\text{SO}_4^{2-}$ , another ubiquitous species in deep groundwater, on the corrosion behavior of NiCu low alloy steel during immersion in simulated deep groundwater environments using in situ electrochemical measurements and surface analysis techniques. Results show that  $\text{SO}_4^{2-}$  addition promotes substrate dissolution during the initial immersion stage. In later stages,  $\text{SO}_4^{2-}$  weakens the protectiveness of formed films, resulting in active dissolution prevailing on the electrode surface rather than prepassivation behavior. Both concentrated  $\text{SO}_4^{2-}$  and  $\text{HCO}_3^-$  promote the formation of  $\text{Fe}_6(\text{OH})_{12}\text{CO}_3$ . The main corrosion products consist of  $\alpha$ - $\text{FeOOH}$ ,  $\text{Fe}_3\text{O}_4$ , and  $\text{Fe}_6(\text{OH})_{12}\text{CO}_3$ , with uniform corrosion observed as the primary corrosion morphology.

**Keywords:** low alloy steel, rust layer,  $\text{HCO}_3^-$ ,  $\text{SO}_4^{2-}$

## 1. Introduction

Low-carbon steel has been considered a candidate material for high-level radioactive waste disposal canisters due to its low susceptibility to localized corrosion and low manufacturing cost [1-4]. However, compared with other candidate materials such as copper, titanium alloys, and nickel-based alloys, low-carbon steel exhibits a higher corrosion rate [5-7], resulting in shorter service life and severely limiting its practical application. Alloying treatment represents a feasible approach to improve corrosion resistance and reduce the average corrosion rate of low-carbon steel without substantially increasing cost.

Deep groundwater in China's preselected high-level waste geological disposal

sites typically contains both  $\text{HCO}_3^-$  and  $\text{Cl}^-$  [8]. Chloride ions exert strong aggressive effects on canister materials, readily inducing localized corrosion that seriously threatens canister service life and safe waste disposal. Therefore, alloyed low-carbon steel must first demonstrate satisfactory corrosion resistance in chloride-containing environments. NiCu low alloy steel, as a marine-grade steel, has exhibited excellent corrosion performance in high-chloride environments such as seawater splash zones and marine atmospheric conditions [9-11]. Consequently, previous work by our research group [12-16] has investigated NiCu low alloy steel as a candidate canister material, examining its corrosion evolution behavior in simulated groundwater environments—specifically deaerated  $\text{NaHCO}_3$  solutions with and without chloride—and comparing it with low-carbon steel behavior under identical conditions. Results demonstrated that NiCu low alloy steel corrodes at a significantly lower rate than low-carbon steel while showing markedly improved resistance to localized corrosion.

Nevertheless, the influence of  $\text{SO}_4^{2-}$ , another major aggressive ion in deep groundwater environments, on the corrosion behavior of NiCu low alloy steel remains unreported. Therefore, this work primarily investigates the corrosion behavior of NiCu low alloy steel in simulated groundwater solutions containing  $\text{SO}_4^{2-}$  using in situ electrochemical monitoring methods to understand how  $\text{SO}_4^{2-}$  affects the active/passive corrosion mode during long-term corrosion processes.

## 2. Experimental Methods

A three-electrode system was employed in this study. The test material was NiCu low alloy steel with the following main chemical composition (mass fraction, %): Ni 3, Cu 0.3, C 0.21, Si 0.21, Mn 0.58, S 0.0036, P 0.017, and Fe balance. Sample dimensions were 10 mm × 10 mm × 3 mm, with a working electrode area of 100 mm<sup>2</sup>; all other surfaces were encapsulated in epoxy resin. All samples were ground sequentially with sandpaper to 800 grit, rinsed with deionized water, degreased with ethanol, and dried before testing. The reference electrode was a saturated calomel electrode (SCE), and the counter electrode was a platinum sheet. The electrolyte solutions consisted of x mol/L  $\text{NaHCO}_3$  + y mol/L  $\text{Na}_2\text{SO}_4$ , where x = 0.05, 0.10 and y = 0.02, 0.05, 0.10; the pH was 8.33. All solutions were prepared using analytical-grade reagents and distilled water.

Prior to experiments, high-purity  $\text{N}_2$  (99.999%) was continuously purged into the sealed electrolytic cell containing the electrolyte solution for deoxygenation. Simultaneously, the sample surface was lightly polished on 800-grit sandpaper with the same electrolyte solution to remove surface films before immediate immersion into the cell. After 30 minutes of continued  $\text{N}_2$  purging, experiments commenced, with a water-sealed bottle maintaining  $\text{N}_2$  atmosphere in the cell headspace throughout the test period. Polarization curves were measured using a PARSTAT 2273 electrochemical workstation. After the open-circuit potential stabilized, scans were conducted from -1.0 V to 0.4 V at a rate of 10

mV/min. Long-term in situ corrosion potential monitoring was performed using an HA-151A potentiostat. During monitoring, electrochemical impedance spectroscopy (EIS) measurements were periodically conducted using the PAR-STAT 2273 workstation over a frequency range of 0.01 Hz to 100 kHz. All potentials reported in this work are relative to SCE.

After immersion testing, NiCu low alloy steel samples were removed, dried under high-purity N<sub>2</sub> flow, and sealed for preservation. Corrosion products formed on sample surfaces were analyzed and identified using a Rigaku-D/max 2500 PC X-ray diffractometer (XRD). Subsequently, corrosion products were removed using a pickling solution (20 g (CH<sub>2</sub>)<sub>6</sub>N<sub>4</sub> + 500 mL HCl + 500 mL H<sub>2</sub>O), and surface corrosion morphologies were examined using an FEI XL-30FEG scanning electron microscope (SEM).

### 3. Results and Discussion

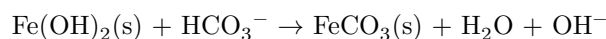
#### 3.1 Polarization Behavior

Figure 1 [Figure 1: see original paper] shows the polarization curves of NiCu low alloy steel in deaerated 0.05 and 0.10 mol/L NaHCO<sub>3</sub> solutions with various SO<sub>4</sub><sup>2-</sup> concentrations. The two solid lines represent results in the corresponding blank NaHCO<sub>3</sub> solutions [15,16]. In both NaHCO<sub>3</sub> solutions, NiCu low alloy steel exhibits similar polarization behavior: hydrogen evolution dominates the cathodic polarization, while anodic polarization shows a transition from active dissolution at low potentials to stable passivation at high potentials, passing through three oxidation peaks designated P1, P2, and P3 in order of increasing peak potential (EP1, EP2, and EP3, respectively). Based on corrosion product composition obtained by Dong et al. [17] for low-carbon steel under various potentiostatic polarization conditions in oxygen-free NaHCO<sub>3</sub> solutions and corresponding potential-pH diagrams, peaks P1, P2, and P3 correspond to transformations from Fe to Fe(II) corrosion products, Fe(II) to Fe(II/III) corrosion products, and Fe(II/III) to Fe(III) corrosion products, respectively.

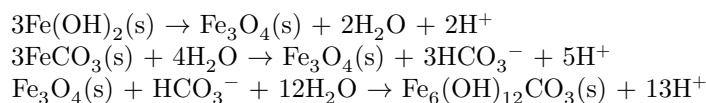
Initially, in the active region where the scan potential E lies between the corrosion potential E<sub>corr</sub> and EP1, the corrosion products on the electrode surface consist primarily of a precursor passive film of Fe(OH)<sub>2</sub> [18,19]:



Under the influence of HCO<sub>3</sub><sup>-</sup>, divalent iron carbonates may also form on the electrode surface:



As the scan potential continues to increase positively, the protectiveness of the precursor passive film strengthens. When E > EP1, the corrosion current density decreases. Then, near EP2, Fe(II) products begin transforming into Fe(II/III) corrosion products:



Among these,  $\text{Fe}_3\text{O}_4$  can exist stably in the passive film and serves as an effective component, whereas  $\text{Fe}_6(\text{OH})_{12}\text{CO}_3$  is relatively unstable and readily oxidizes to Fe(III) corrosion products. Finally, near EP3, Fe(II/III) products transform to Fe(III) corrosion products [16]:



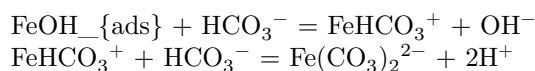
The addition of various  $\text{SO}_4^{2-}$  concentrations to these two  $\text{NaHCO}_3$  solutions produces minimal changes in  $E_{\text{corr}}$  and the cathodic portions of the polarization curves but significantly affects the anodic portions. First,  $\text{SO}_4^{2-}$  addition shifts the entire anodic polarization curve rightward, indicating increased anodic corrosion current density. Second, added  $\text{SO}_4^{2-}$  alters the anodic polarization behavior, particularly in the high-potential region. In the lower-concentration (0.05 mol/L)  $\text{NaHCO}_3$  solution (Fig. 1a), when the  $\text{SO}_4^{2-}$  addition is 0.02 mol/L, the anodic polarization behavior after active dissolution and peaks P1 and P2 shows a sudden increase in corrosion current density at  $E = -0.49$  V, followed by secondary passivation at  $E = -0.144$  V with a final passive current density of approximately  $0.3 \text{ mA/cm}^2$ . When  $\text{SO}_4^{2-}$  reaches 0.05 mol/L, the anodic polarization behavior no longer exhibits obvious passivation characteristics; after a continuously increasing active dissolution region, the sample shows limiting diffusion characteristics in the high-potential region, with diffusion current density increasing with  $\text{SO}_4^{2-}$  concentration.

In the higher-concentration (0.10 mol/L)  $\text{NaHCO}_3$  solution (Fig. 1b), the influence of  $\text{SO}_4^{2-}$  on the anodic polarization curve diminishes. In the low-potential region, samples with different  $\text{SO}_4^{2-}$  concentrations still experience peaks P1 and P2 after the active region. In the high-potential region, the anodic polarization behavior shows features different from those in blank  $\text{NaHCO}_3$  solutions: after peak P2, the polarization curves all exhibit a stage of rapid corrosion current density increase, with no secondary passivation occurring as the scan potential continues to increase, ultimately showing obvious limiting diffusion behavior. The limiting diffusion current densities in solutions with 0.02, 0.05, and 0.10 mol/L  $\text{SO}_4^{2-}$  stabilize at approximately 43.6, 107.7, and 480.3  $\text{A/cm}^2$ , respectively. These results demonstrate that  $\text{SO}_4^{2-}$  addition in  $\text{NaHCO}_3$  solutions inhibits passive film formation on the electrode surface, with the effect becoming more pronounced as  $\text{SO}_4^{2-}$  concentration increases. In lower-concentration  $\text{NaHCO}_3$  solutions, high  $\text{SO}_4^{2-}$  concentrations hinder passive film formation on the substrate, maintaining the electrode corrosion mode as active dissolution; in higher-concentration  $\text{NaHCO}_3$  solutions,  $\text{SO}_4^{2-}$  addition damages the protectiveness of surface product films, increasing corrosion current density.

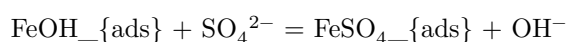
### 3.2 Open-Circuit Potential Evolution

Since  $\text{SO}_4^{2-}$  demonstrates more pronounced destructive effects on passive films at high concentrations, solutions containing 0.10 mol/L  $\text{Na}_2\text{SO}_4$  in both 0.05 and 0.10 mol/L  $\text{NaHCO}_3$  were selected to study the corrosion behavior evolution of NiCu low alloy steel during immersion. The solid lines in Figure 2 [Figure 2: see original paper] show the open-circuit potential variation with immersion time in these two test solutions, while the dashed lines represent results in corresponding blank  $\text{NaHCO}_3$  solutions [15,16]. All open-circuit potential curves generally undergo three stages: a slow rise, a rapid positive shift, and fluctuation before eventual stabilization. Without  $\text{SO}_4^{2-}$  addition, as  $\text{NaHCO}_3$  concentration increases from 0.05 to 0.10 mol/L, the first stage duration shortens significantly (from 40 to 25 days), and the stable potential in the third stage increases from -0.40 V to -0.28 V. Based on corresponding polarization curves, both ultimately reach the prepassivation region, with improved product film protectiveness at higher  $\text{NaHCO}_3$  concentrations.

Although  $\text{SO}_4^{2-}$  addition has minimal effect on the initial open-circuit potential, it introduces two notable changes in subsequent evolution. First, compared with  $\text{SO}_4^{2-}$ -free solutions, the first stage duration shortens considerably. According to Bockris et al. [18],  $\text{FeOH}_{\text{ads}}$  exists as an intermediate product during Fe dissolution to  $\text{Fe}^{2+}$ . When  $\text{HCO}_3^-$  is present in solution, it can react directly with  $\text{FeOH}_{\text{ads}}$ , promoting substrate dissolution [19,20]:



Both  $\text{FeHCO}_3^+$  and  $\text{Fe}(\text{CO}_3)_2^{2-}$  are soluble species that further ionize to  $\text{Fe}^{2+}$ . When  $\text{SO}_4^{2-}$  is also present, it can react with  $\text{FeOH}_{\text{ads}}$ :



The generated  $\text{FeSO}_4_{\text{ads}}$  also transforms to  $\text{Fe}^{2+}$ . Therefore,  $\text{SO}_4^{2-}$  addition promotes substrate corrosion during initial immersion, resulting in more corrosion product deposition on the electrode surface. These products form galvanic couples with the metal substrate, further driving the open-circuit potential positive and causing the second stage to occur earlier. The second change is that 0.10 mol/L  $\text{SO}_4^{2-}$  addition stabilizes the final open-circuit potential at approximately -0.59 V in both 0.05 and 0.10 mol/L  $\text{NaHCO}_3$  solutions, significantly lower than in corresponding blank  $\text{NaHCO}_3$  solutions [15,16]. Based on polarization curves (Fig. 1), in 0.05 mol/L  $\text{NaHCO}_3$  + 0.10 mol/L  $\text{Na}_2\text{SO}_4$  solution, the final stable open-circuit potential lies in the active region, indicating predominant substrate active dissolution; in 0.10 mol/L  $\text{NaHCO}_3$  + 0.10 mol/L  $\text{Na}_2\text{SO}_4$  solution, the final stable open-circuit potential lies between EP1 and EP2, placing the electrode surface in a prepassivation state. Thus,  $\text{SO}_4^{2-}$  addition inhibits passive film formation, particularly evident in lower-concentration  $\text{NaHCO}_3$  solutions.

### 3.3 Electrochemical Impedance Spectroscopy

To further investigate the corrosion behavior evolution of NiCu low alloy steel during immersion, in situ EIS monitoring was conducted. During the second stage, the rapid positive shift of open-circuit potential indicates drastic changes in electrode surface state that violate “stability conditions” [21]; therefore, measurements were not performed during this stage. Figure 3 [Figure 3: see original paper] presents EIS results for the first and third stages of immersion in 0.05 mol/L NaHCO<sub>3</sub> + 0.10 mol/L Na<sub>2</sub>SO<sub>4</sub> solution.

After 1 day of immersion, the Bode phase angle plot (Fig. 3a) shows a broad, symmetric phase angle peak of approximately 69° at a peak frequency near 4.6 Hz, with a slight upward trend in the low-frequency region (around 10 mHz). The Bode magnitude plot (Fig. 3b) reveals that the low-frequency impedance RLF reaches its maximum value of approximately 5300 Ω · cm<sup>2</sup>. As immersion time extends, the phase angle peak remains symmetric while gradually shifting to lower frequencies (Fig. 3a). After 32 days, the peak frequency has moved to approximately 0.03 Hz with a peak value of about 72°. RLF decreases progressively with time (Fig. 3b), reaching only approximately 630 Ω · cm<sup>2</sup> after 32 days. The high-frequency impedance RHF (at 1 kHz) shows little variation, fluctuating between 16–20 Ω · cm<sup>2</sup>. After experiencing the rapid open-circuit potential increase in the second stage, the open-circuit potential stabilizes in the third stage. Correspondingly, Figs. 3c and 3d show that EIS results in the later third stage overlap. Similar to the first stage, third-stage EIS (Fig. 3c) exhibits only a symmetric phase angle peak in the low-frequency region besides high-frequency phase shift, but with the peak frequency shifting slightly higher to approximately 0.13 Hz and a peak value of about 62°. As shown in Fig. 3d, RLF increases to approximately 1000 Ω · cm<sup>2</sup>. This indicates that corrosion products deposited on the electrode surface during later immersion stages do not possess passive characteristics, and the electrode surface remains in an active dissolution state.

Figure 4 [Figure 4: see original paper] shows EIS results for the first and third stages in 0.10 mol/L NaHCO<sub>3</sub> + 0.10 mol/L Na<sub>2</sub>SO<sub>4</sub> solution. After 1 day of immersion, the Bode phase angle plot (Fig. 4a) also displays a broad, symmetric phase angle peak of approximately 70° near 6.3 Hz, with a slight upward trend in the low-frequency region (around 10 mHz). As immersion time extends, the phase angle peak gradually shifts to lower frequencies. After 14 days, the phase angle plot begins to show an asymmetric peak in the low-frequency region, generally resulting from the superposition of two peaks. This suggests that, unlike in 0.05 mol/L NaHCO<sub>3</sub> + 0.10 mol/L Na<sub>2</sub>SO<sub>4</sub> solution, the corrosion products generated on the electrode surface during the later first stage in 0.10 mol/L NaHCO<sub>3</sub> + 0.10 mol/L Na<sub>2</sub>SO<sub>4</sub> solution likely already function as a barrier layer. The magnitude plot (Fig. 4b) shows RLF of approximately 2887 Ω · cm<sup>2</sup> after 1 day, increasing after 4 days, then gradually decreasing with prolonged immersion to about 1203 Ω · cm<sup>2</sup> at 20 days. RHF remains relatively stable throughout immersion, fluctuating between 14–17 Ω · cm<sup>2</sup>. As the elec-

trode surface state stabilizes in the third stage, the impedance spectra also show overlapping patterns in this stage (Figs. 4c and 4d). Similar to the later first-stage results, third-stage phase angle plots all show asymmetric peaks in the low-frequency region (Fig. 4c). As shown in Fig. 4d, RLF in the third stage varies between  $813\text{--}1158 \Omega \cdot \text{cm}^2$ .

Generally, the number of peaks in Bode phase angle plots (excluding high-frequency phase shift) corresponds to the number of time constants [21]. Based on Figs. 3 and 4, two equivalent circuits shown in Fig. 5 [Figure 5: see original paper] were selected for fitting the impedance spectra. The circuit in Fig. 5a was used to fit EIS displaying only one time constant, including all impedance data measured in  $0.05 \text{ mol/L NaHCO}_3 + 0.10 \text{ mol/L Na}_2\text{SO}_4$  solution and data from the first 8 days in  $0.10 \text{ mol/L NaHCO}_3 + 0.10 \text{ mol/L Na}_2\text{SO}_4$  solution. In this circuit, QHF represents high-frequency capacitance, Re represents electrolyte resistance, Qdl represents double-layer capacitance, and Rct represents charge transfer resistance. Additionally, Sherar et al. [22] demonstrated that incorporating Warburg impedance in series with charge transfer resistance improves fitting accuracy in the low-frequency region and reflects the hindrance of corrosion product films to ion transport processes. Therefore, Warburg impedance (denoted as W) was also included in Fig. 5a. Since W and QHF are only used in fitting some impedance spectra, they are connected with dashed lines. The circuit in Fig. 5b was used to fit impedance spectra displaying two time constants, specifically data measured after 14 days in  $0.10 \text{ mol/L NaHCO}_3 + 0.10 \text{ mol/L Na}_2\text{SO}_4$  solution, where Qcp and Rcp represent the capacitance and resistance of the deposited corrosion product layer, respectively.

For constant phase elements (CPE) in Fig. 5 (QHF, Qdl, and Qcp), their impedance  $Z_Q$  is a function of angular frequency  $\omega$ :

$$Z_Q = Y_0^{-1}(j\omega)^{-n}$$

Thus, the equivalent element Q has two parameters:  $Y_0$  with units of  $\text{S} \cdot \text{s}^n \cdot \text{cm}^{-2}$ , and the dimensionless exponent  $n$ . Depending on the  $n$  value, CPE can represent inductance ( $n = -1$ ), resistance ( $n = 0$ ), Warburg impedance ( $n = 0.5$ ), or pure capacitance ( $n = 1$ ). Specific fitting results are listed in Tables 1 and 2. The evolution of Rct with immersion time is shown in Fig. 6 [Figure 6: see original paper], with dashed lines indicating Rct variations in corresponding pure  $\text{NaHCO}_3$  solutions [15,16].

Table 1 shows that during the first stage (first 32 days) in  $0.05 \text{ mol/L NaHCO}_3 + 0.10 \text{ mol/L Na}_2\text{SO}_4$  solution, Re fluctuates around  $18 \Omega \cdot \text{cm}^2$ . Rct first decreases then increases, consistent with the trend in corresponding blank  $\text{NaHCO}_3$  solutions (Fig. 6a). During early immersion, anion intrusion enhances polarization, decreasing Rct and facilitating the corrosion process; as corrosion products gradually deposit, the corrosion process becomes inhibited and Rct increases. Additionally, ndl remains above 0.8 throughout the first stage, while  $Y_{0,dl}$  increases with time, indicating that the double-layer interface maintains good capacitive characteristics that increase with corrosion progression and product deposition

[21]. In the third stage (after 44 and 50 days),  $R_e$  shows little change,  $n_{dl}$  remains above 0.8, while  $Y_{0,dl}$  and  $R_{ct}$  are lower than the 32-day values. This indicates that corrosion products deposited on the sample surface in the third stage cannot effectively hinder the corrosion process; instead, they accelerate corrosion by forming galvanic couples with the metal substrate, increasing the corrosion rate. Moreover, compared with blank  $\text{NaHCO}_3$  solutions, the third-stage  $R_{ct}$  decreases after adding  $0.10 \text{ mol/L SO}_4^{2-}$ , significantly promoting the corrosion process.

As shown in Table 2 and Fig. 6b, in  $0.10 \text{ mol/L NaHCO}_3 + 0.10 \text{ mol/L Na}_2\text{SO}_4$  solution, the third-stage  $R_{ct}$  is also much lower than in the corresponding blank  $\text{NaHCO}_3$  solution. However, unlike the previous case, the impedance spectra in the later first stage (after 14 days) in  $0.10 \text{ mol/L NaHCO}_3 + 0.10 \text{ mol/L Na}_2\text{SO}_4$  solution reveal the presence of another capacitance-resistance pair  $Q_{cp}$  and  $R_{cp}$  in addition to  $Q_{dl}$  and  $R_{ct}$ . With time extension,  $R_{cp}$ ,  $n_{cp}$ , and  $Y_{0,cp}$  all gradually increase; third-stage  $R_{ct}$  does not decrease compared with the first stage, and  $Y_{0,dl}$  also increases. Comprehensive comparison with polarization curve results indicates that increasing  $\text{NaHCO}_3$  concentration from 0.05 to 0.10 mol/L facilitates the formation of passive corrosion product films, causing the film to transition from porous to dense and thereby providing some hindrance to aggressive ion intrusion.

### 3.4 Surface Analysis

Figure 7 [Figure 7: see original paper] shows XRD spectra of corrosion products formed on NiCu low alloy steel after immersion tests. The corrosion products in both  $0.05 \text{ mol/L NaHCO}_3 + 0.10 \text{ mol/L Na}_2\text{SO}_4$  and  $0.10 \text{ mol/L NaHCO}_3 + 0.10 \text{ mol/L Na}_2\text{SO}_4$  solutions consist mainly of  $\alpha\text{-FeOOH}$ ,  $\text{Fe}_3\text{O}_4$ , and  $\text{Fe}_6(\text{OH})_{12}\text{CO}_3$ . In  $0.05 \text{ mol/L NaHCO}_3 + 0.10 \text{ mol/L Na}_2\text{SO}_4$  solution,  $\text{Fe}_3\text{O}_4$  diffraction peaks are relatively strong while  $\text{Fe}_6(\text{OH})_{12}\text{CO}_3$  peaks are weak; conversely, in  $0.10 \text{ mol/L NaHCO}_3 + 0.10 \text{ mol/L Na}_2\text{SO}_4$  solution,  $\text{Fe}_3\text{O}_4$  peaks are weak while  $\text{Fe}_6(\text{OH})_{12}\text{CO}_3$  peaks are strong. This indicates that increased  $\text{HCO}_3^-$  concentration promotes  $\text{Fe}_6(\text{OH})_{12}\text{CO}_3$  formation [23-25]. Compared with results in blank  $\text{NaHCO}_3$  solutions [15,16],  $\text{SO}_4^{2-}$  addition also promotes  $\text{Fe}_6(\text{OH})_{12}\text{CO}_3$  formation because  $\text{SO}_4^{2-}$  promotes substrate dissolution (reactions (11)-(13)), increasing the conversion amount of  $\text{Fe}_6(\text{OH})_{12}\text{CO}_3$  (reaction (9)).

Surface corrosion morphologies of NiCu low alloy steel samples after removing surface corrosion products following immersion tests are shown in Figure 8 [Figure 8: see original paper]. Figures 8a and 8b reveal that after 56 days of immersion in  $0.05 \text{ mol/L NaHCO}_3 + 0.10 \text{ mol/L Na}_2\text{SO}_4$  solution, the surface morphology is primarily uniform corrosion. Compared with results in blank  $\text{NaHCO}_3$  solutions, the sample surface shows more pronounced height variations but significantly fewer and smaller corrosion pits. Figure 8c shows that after 43 days in  $0.10 \text{ mol/L NaHCO}_3 + 0.10 \text{ mol/L Na}_2\text{SO}_4$  solution, the sample surface is relatively flat, also exhibiting uniform corrosion morphology without obvious

pitting. Only at high magnification can fine corrosion pits be observed, as shown in Fig. 8d. Thus, even with protective corrosion product film formation after long-term immersion in 0.10 mol/L  $\text{NaHCO}_3$  + 0.10 mol/L  $\text{Na}_2\text{SO}_4$  solution, the corrosion mode remains uniform corrosion.

These discussions demonstrate that during initial corrosion stages, both  $\text{HCO}_3^-$  and  $\text{SO}_4^{2-}$  can promote substrate dissolution (reactions (11)-(13)). However, regarding passive film formation in later stages,  $\text{HCO}_3^-$  has a promotional effect [19,20] while  $\text{SO}_4^{2-}$  exerts an inhibitive effect, creating competition between the two species. Due to its strong electronegativity,  $\text{SO}_4^{2-}$  readily adsorbs at electrode surface sites, preventing  $\text{HCO}_3^-$  from accumulating in large quantities and thereby hindering passive film formation. Adding 0.10 mol/L  $\text{SO}_4^{2-}$  to 0.05 mol/L  $\text{NaHCO}_3$  solution maintains the electrode surface in an active dissolution state with a relatively high corrosion rate. When  $\text{HCO}_3^-$  concentration is higher (0.10 mol/L  $\text{NaHCO}_3$ ), the destructive effect of  $\text{SO}_4^{2-}$  is suppressed, but the corrosion rate still increases significantly compared with blank  $\text{NaHCO}_3$  solutions. Consequently, uniform corrosion morphology dominates the sample surfaces after immersion in both solutions.

#### 4. Conclusions

1. During initial immersion of NiCu low alloy steel in deaerated 0.05 and 0.10 mol/L  $\text{NaHCO}_3$  solutions, adding 0.10 mol/L  $\text{SO}_4^{2-}$  accelerates corrosion compared with blank  $\text{NaHCO}_3$  solutions.
2. During later immersion stages, added 0.10 mol/L  $\text{SO}_4^{2-}$  hinders passive film formation on NiCu low alloy steel surfaces. In 0.05 mol/L  $\text{NaHCO}_3$  solution, the electrode surface remains in an active dissolution state with a relatively high corrosion rate; in 0.10 mol/L  $\text{NaHCO}_3$  solution, the protectiveness of surface corrosion products decreases, increasing the corrosion rate.
3. After immersion tests, corrosion products on sample surfaces consist mainly of  $\alpha\text{-FeOOH}$ ,  $\text{Fe}_3\text{O}_4$ , and  $\text{Fe}_6(\text{OH})_{12}\text{CO}_3$ . Both increased  $\text{SO}_4^{2-}$  and  $\text{HCO}_3^-$  concentrations promote  $\text{Fe}_6(\text{OH})_{12}\text{CO}_3$  formation. The surface morphology remains primarily uniform corrosion.

#### References

- [1] Taniguchi N, Suzuki H, Kawasaki M, Naito M, Kobayashi M, Takahashi R, Asano H. *Corros Eng Sci Technol*, 2011; 46: 117
- [2] Kursten B, Druyts F, Macdonald D D, Smart N R, Gens R, Wang L, Weetjens E, Govaerts J. *Corros Eng Sci Technol*, 2011; 46: 91
- [3] Macdonald D D, Urquidi-Macdonald M, Engelhardt G R, Azizi O, Saleh A, Almazooqi A, Rosas-Camacho O. *Corros Eng Sci Technol*, 2011; 46: 98
- [4] Féron D, Crusset D, Gras J M. *J Nucl Mater*, 2008; 379: 16
- [5] Bennett D G, Gens R. *J Nucl Mater*, 2008; 379: 1

- [6] King F, Padovani C. Corros Eng Sci Technol, 2011; 46: 82
- [7] King F. Corrosion, 2013; 69: 986
- [8] Guo Y H, Wang J, Lv C H, Liu S F, Zhong Z H. Earth Sci Front, 2005; 12(Suppl): 117
- [9] Cao G L, Li G M, Chen S, Chang W S, Chen X Q. Acta Metall Sin, 2011; 47: 145
- [10] Matsushima I, Translated by Jing Y K. Low-Alloy Corrosion Resistant Steels: A History of Development, Application and Research. Beijing: Metallurgical Industry Press, 2004: 100
- [11] Kihira H, Kimura M. Corrosion, 2011; 67: 1
- [12] Yang J F, Dong J H, Ke W. Acta Metall Sin, 2011; 47: 1321
- [13] Wen H L, Dong J H, Ke W, Chen W J, Yang J F, Chen N. Acta Metall Sin, 2014; 50: 275
- [14] Lu Y F, Yang J F, Dong J H, Ke W. Acta Metall Sin, 2015; 51: 440
- [15] Lu Y F, Dong J H, Ke W. J Mater Sci Technol, accepted.
- [16] Lu Y F, Dong J H, Ke W. J Mater Sci Technol, doi:10.1016/j.jmst.2014.10.013
- [17] Dong J H, Nishimura T, Kodama T. MRS Symp Process, 2002; 713: 105
- [18] Bockris J O M, Drazic D, Despic A R. Electrochim Acta, 1961; 4: 325
- [19] Davies D H, Burstein G T. Corrosion, 1980; 36: 416
- [20] Burstein G T, Davies D H. Corros Sci, 1980; 20: 1143
- [21] Cao C N, Zhang J Q. Introduction of Electrochemical Impedance Spectroscopy. Beijing: Science Press, 2002: 135
- [22] Sherar B W A, Keech P G, Qin Z, King F, Shoesmith D W. Corrosion, 2010; 66: 045001-1
- [23] Genin J M R, Bourrie G, Trolard F, Abdelmoula M, Jaffrezic A, Refait P, Maitre V, Humbert B, Herbillon A. Environ Sci Technol, 1988; 32: 1058
- [24] Larroumet D, Greenfield D, Akid R, Yarwood J. J Raman Spectrosc, 2008; 39: 1740
- [25] Drissi S H, Refait P, Abdelmoula M, Genin J M R. Corros Sci, 1995; 37: 2025

*Note: Figure translations are in progress. See original paper for figures.*

*Source: ChinaXiv – Machine translation. Verify with original.*